

A Comparison of X-ray and Strong Lensing Properties of Simulated X-ray Clusters

Matthias Bartelmann¹ and Matthias Steinmetz^{1,2}

¹Max-Planck-Institut für Astrophysik, Karl-Schwarzschild-Straße 1, D-85748 Garching, Germany;

²Present address: Department of Astronomy, University of California, Berkeley, CA 94720, USA

Abstract. We use gas-dynamical simulations of galaxy clusters to compare their X-ray and strong lensing properties. Special emphasis is laid on mass estimates. The cluster masses range between $6 \times 10^{14} M_{\odot}$ and $4 \times 10^{15} M_{\odot}$, and they are examined at redshifts between 1 and 0. We compute the X-ray emission of the intracluster gas by thermal bremsstrahlung, add background contamination, and mimic imaging and spectral observations with current X-ray telescopes. Although the β model routinely provides excellent fits to the X-ray emission profiles, the derived masses are typically biased low because of the restricted range of radii within which the fit can be done. For β values of $\sim 2/3$, which is the average in our numerically simulated sample, the mass is typically underestimated by ~ 40 per cent. The masses of clusters which exhibit pronounced substructure are often substantially underestimated. We suggest that the ratio between peak temperature and emission-weighted average cluster temperature may provide a good indicator for ongoing merging and, therefore, for unreliable mass estimates. X-ray mass estimates are substantially improved if we fit a King density profile rather than the β model to the X-ray emission, thereby dropping the degree of freedom associated with β . Clusters selected for their strong lensing properties are typically dynamically more active than typical clusters. Bulk flows in the intracluster gas contain a larger than average fraction of the internal energy of the gas in such objects, hence the measured gas temperatures are biased low. The bulk of the optical depth for arc formation is contributed by clusters with intermediate rather than high X-ray luminosity. Arcs occur predominantly in clusters which exhibit substructure and are not in an equilibrium state. Finally we explain why the X-ray emission of some observed arc clusters is cooler than predicted from the arc geometry. All clusters for which this happens in our simulations show structure in velocity space, indicating ongoing merging along the line-of-sight. The temperature discrepancy is probably a projection effect.

Key words: Galaxies: clustering – Cosmology: dark matter – X-rays: general

1. Introduction

Until ten years ago, masses of galaxy clusters were mainly determined using the kinematics of cluster galaxies. Although these mass estimates are fairly crude (due mainly to small number statistics), they already provided compelling evidence that most of the mass of galaxy clusters is dark and is not concentrated in the cluster galaxies themselves (Zwicky 1933). Within the last decade, this method was complemented by two new, powerful methods based on the X-ray emission of galaxy clusters and on their gravitational lens effects. Similar to kinematic mass estimates, mass estimates based on X-ray data generally rely on several *a priori* assumptions, viz. (i) that the cluster mass distribution is spherically symmetric, (ii) that the X-ray emitting gas is in hydrostatic equilibrium with the dark-matter potential, and (iii) that the X-ray emitting gas is in thermal equilibrium, in particular that its pressure is dominated by thermal pressure. X-ray observations imply that the total mass of the X-ray emitting gas is larger by about a factor five than that of the cluster galaxies, but that the total baryonic mass from gas and galaxies together is still smaller than the total cluster mass by about a factor of five to ten.

Gravitational lensing of background galaxies opens a much more direct way to infer cluster masses. Especially mass estimates based on weak lensing, i.e. on the small image distortions of background galaxies, appear very promising (e.g., Kaiser & Squires 1993; Bonnet, Mellier, & Fort 1994; Seitz & Schneider 1995; Broadhurst, Taylor, & Peacock 1995; Squires & Kaiser 1995; and references therein). It turns out, however, that the power of weak lensing is more in obtaining the *morphology* of the mass distribution within a galaxy cluster, while it is much more difficult to deduce reliable estimates of the total mass (e.g., Squires & Kaiser 1995; Wilson, Cole, & Frenk 1995; Seitz & Schneider 1996; Bartelmann et al. 1996; and references therein). In addition, the essentially statistical analysis of weak-lensing effects requires to average over background galaxy images and therefore has a limited spatial resolution. Close to cluster centers, where most of the X-rays are emitted, it is therefore difficult to produce well-resolved mass maps. In addition, the contamination of the background galaxy population by cluster galaxies is more severe close to the cluster centers. Hence, while weak lensing can be expected to yield important information about the outer parts of galaxy clusters, strong lensing may provide more stringent constraints on their central regions. At present, the masses inferred from these three methods, viz. galaxy kinematics, X-ray emission, and gravitational lensing, agree to within about a factor of two, but a systematic comparison still needs to be done.

All observations performed so far demonstrate that the masses of galaxy clusters are strongly dominated by dark matter. Although the ratio between the total masses of baryonic and dark matter within galaxy clusters is still a matter of debate (e.g., whether the hidden mass in galaxy clusters is sufficient to account for a high- Ω_0 universe), there is general agreement that this ratio is at least five. From the theoretical point of view, such observations were complemented by N -body and, in the more recent past, hydrodynamical simulations (Thomas & Couchman 1992; Schindler & Müller 1993; Katz & White 1993; Cen & Ostriker 1994; Bryan et al. 1994; Navarro, Frenk, & White 1995a; Evrard, Metzler, & Navarro 1995). Gas-dynamical simulations performed so far have shown that under most circumstances the mass estimates based on the assumptions of spherical symmetry and hydrostatic equilibrium are reasonably accurate, especially within an intermediate range of cluster radii. Only in clusters which exhibit pronounced substructure is this assumption obviously and demonstrably invalid. In addition, the simulations have shown that the mass of clusters which are undergoing a merging event is systematically underestimated because a fraction of the energy of the gas is in the kinetic energy of bulk motions rather than in thermal energy (Navarro et al. 1995a). Therefore the temperature and consequently also the mass of such clusters are underestimated. Nevertheless, Evrard et al. (1995) emphasize that for clusters which do not clearly exhibit strong substructure, the mass estimates are accurate to within 20 per cent and do not show a systematic bias. They also argue that the accuracy of mass estimates can be further improved using scaling relations. Their analysis was however done under idealizing conditions in so far as (1) the emission-weighted temperature of the simulated clusters was taken from the simulations rather than from the cluster spectra, (2) the X-ray images were analyzed out to large radii, and (3) only clusters at low redshift were considered. For comparison with results from gravitational lensing, however, clusters at intermediate redshifts need to be studied because of the low lensing efficiency of low-redshift clusters.

It is so far unclear which kinds of X-ray emitting clusters are selected by the strong lensing effect. In order to be able to produce large arcs, clusters have to be critical to lensing, which means that a certain combination of their surface-mass density and shear field must exceed a critical limit. This criterion has often been interpreted such that the lensing clusters have to be the most massive and hence most luminous and hottest X-ray clusters. It turns out, however, that some of the clusters which show the most spectacular arcs such as Abell 370 are only moderate X-ray emitters, while other more prominent X-ray sources such as Abell 2163 are only moderately strong lenses. Moreover, recent numerical studies (Bartelmann, Steinmetz, & Weiss 1995) have shown that the probability for a cluster to form large arcs is significantly larger if the cluster is substructured because the tidal field of a cluster with substructure is larger than that of a spherically symmetric cluster, and the number of cusps which are crucial for the formation of large arcs in the caustic curves of cluster lenses is significantly enhanced by asymmetries in the lens. Substructured clusters are, however, expected to be far from equilibrium, and this should affect the X-ray properties of those particular lenses. Miralda-Escudé & Babul (1995) in a recent study have found that two of three clusters for which lensing- and X-ray data were available should have a higher temperature to explain their lensing properties than the measured temperature of the X-ray gas. It is important for our understanding of the internal structure of galaxy clusters to identify the reason for such temperature discrepancies.

Apart from the intrinsic interest in masses of galaxy clusters, cluster masses are also of considerable importance for cosmology. For example, a systematic underestimation of cluster mass based on X-ray observations would favor a higher Ω_0 , a higher amplitude of the power spectrum on scales of several Mpc, and it would also render the baryon catastrophe (White et al. 1993; White & Fabian 1995) less severe. Thus it is important to identify possible systematic errors in the estimation of cluster masses.

The present paper compares the X-ray and lensing properties of numerically simulated galaxy clusters. The outline of the paper is as follows. In Sect. 2, we describe our numerical simulations and discuss the properties of our cluster sample. We describe how the X-ray and lensing properties of the cluster sample are simulated and how “detector characteristics” are implemented. Section 3 concentrates on mass estimates as obtained by X-ray “observations” of the cluster sample. Section 4 concentrates on lensing and the properties of X-ray clusters selected for their lensing effect. In Sect. 5 we summarize and discuss our main results and conclusions.

2. Numerical Cluster Simulations

2.1. The Simulations

The simulations were performed with the Smoothed Particle Hydrodynamics (SPH) code GRAPESPH (Steinmetz 1996). The background cosmogony is an $\Omega_0 = 1$, $H_0 = 50 \text{ km s}^{-1}$ CDM model normalized to $\sigma_8 = 1$. The baryon fraction is $\Omega_b = 0.05$. Our choice of the background cosmogony should be interpreted as a convenient way to create a realistic sample of galaxy clusters in different dynamical states, as opposed to trying to assess the merits and shortcomings of high- Ω_0 CDM. As a matter of fact, most of our conclusions below are primarily caused by the hierarchical assembly of galaxy clusters, while the details of the cosmogony are probably of minor importance.

In order to perform simulations with sufficiently high resolution, we applied a multiple mass scheme as described by Katz & White (1993), Navarro et al. (1995a), and Bartelmann, Steinmetz, & Weiss (1995). Based on a coarsely grained N -body simulation in a cube of side length 300 Mpc, the 13 most massive clusters are selected. These clusters are re-simulated in high-resolution runs incorporating the effects of gas dynamics. In contrast to Katz & White (1993), but similar to Evrard et al. (1995) and Navarro et al. (1995a), we do not include radiative cooling processes, mainly because the interplay between gas cooling, feedback processes due to the formation of stars within galaxies, and the limited numerical resolution is not satisfactorily understood. On the other hand, numerical simulations (Evrard et al. 1995; White, Efstathiou, & Frenk 1993) which were performed neglecting radiative cooling show a qualitatively good correspondence between observed and numerically simulated X-ray clusters, though some scaling relations like for example the temperature–luminosity relation of observed clusters are not reproduced (Navarro et al. 1995a). Only thermal sources of gas pressure are taken into account; the possible influence of magnetic pressure is neglected. Nevertheless, we think that numerically simulated galaxy clusters are fair representatives of real clusters in the sense that they reproduce typical amounts of structure and typical varieties of dynamic states. They are a generalization of the commonly used hydrostatic models taking into account asymmetry as well as internal dynamics. However, in spite of imperfections of the modeling, statistical analyses and scaling relations should be applied with caution.

The 13 cluster models projected along the three independent spatial directions at $\sim 8 - 10$ time steps each between redshifts 1 and 0 yield 378 simulated cluster images.

2.2. X-ray Emission

The temperature and density of the SPH gas particles are interpolated to an equidistant grid with the usual SPH procedure (Lucy 1977; Gingold & Monaghan 1977; Monaghan 1992). At a grid point \mathbf{r} , the SPH-averaged density is given by the sum

$$\langle \rho(\mathbf{r}) \rangle = \sum_{i=1}^N m_i W(\mathbf{r} - \mathbf{r}_i; h_i), \quad (1)$$

where i is running over all N particles. The positions, masses, and smoothing lengths of the particles are \mathbf{r}_i , m_i , and h_i , respectively, and $W(\mathbf{r}; h)$ is the SPH smoothing kernel. Given the density, the temperature at the grid position \mathbf{r} is determined by

$$\langle T(\mathbf{r}) \rangle = \sum_{i=1}^N m_i \frac{T(\mathbf{r}_i)}{\rho(\mathbf{r}_i)} W(\mathbf{r} - \mathbf{r}_i; h_i), \quad (2)$$

where $\rho(\mathbf{r}_i)$ is the density of the SPH particle i .

Given temperature and density of the gas in the grid cells, the bremsstrahlung emission of each cell can be computed. It is sufficient for our purposes to include continuum emission only, hence the emissivity is

$$j(T, n_e) = \frac{4C_j}{1+f} \left(\frac{kT}{\text{keV}} \right)^{1/2} \left(\frac{n_e}{\text{cm}^{-3}} \right)^2 \times \left[\exp\left(-\frac{E_a}{kT}\right) - \exp\left(-\frac{E_b}{kT}\right) \right] \frac{\text{erg}}{\text{cm}^3 \text{s}}, \quad (3)$$

where f is the hydrogen fraction by weight of the gas, n_e is its electron number density, and $E_{a,b}$ are the lower and upper bounds of the energy band in which the emission is observed. We choose $f = 0.75$. With the Gaunt factor set to unity,

$$C_j = 2.42 \times 10^{-24}. \quad (4)$$

The number of photons emitted from a grid cell is

$$\gamma(T, n_e) = \frac{4C_\gamma}{1+f} \left(\frac{kT}{\text{keV}} \right)^{-1/2} \left(\frac{n_e}{\text{cm}^{-3}} \right)^2 \times \left[E_1\left(-\frac{E_a}{kT}\right) - E_1\left(-\frac{E_b}{kT}\right) \right] \frac{1}{\text{cm}^3 \text{s}}, \quad (5)$$

where $E_1(x)$ is the exponential integral of the first kind. Here, the constant factor is

$$C_\gamma = 1.51 \times 10^{-15}. \quad (6)$$

The spectrum of the photons is determined by

$$d\gamma(T, n_e) = \frac{4C_\gamma}{1+f} \left(\frac{kT}{\text{keV}} \right)^{-1/2} \left(\frac{n_e}{\text{cm}^{-3}} \right)^2 \times \exp\left(-\frac{E}{kT}\right) \frac{dE}{E} \frac{1}{\text{cm}^3 \text{s}}. \quad (7)$$

The bounds of the energy band, $E_{a,b}$, must be redshifted to the cluster redshift.

Equations (3), (5), and (7) can then be combined to compute the total X-ray luminosity, the X-ray flux, the photon flux, and the photon spectrum observed from the model cluster by a detector specified by its area, its energy band, and its spatial and spectral resolutions. All cluster properties such as their masses are later determined based on photon tables only, giving for each observed photon its position in the detector and its energy. In addition, we add a random X-ray background of $3 \times 10^{-4} \text{ s}^{-1} \text{ arcmin}^{-2}$ to the photon tables. This is lower by about an order of magnitude than the high background of the ROSAT *High-Resolution Imager* (HRI; David et al. 1993), but corresponds approximately to the average background of the ROSAT *Position-Sensitive Proportional Counter* (PSPC; Snowden et al. 1995).

We choose an exposure time of 20 ksec, which we reduce for very bright clusters such that the total number of received photons does not exceed 10^5 . As an immediate consequence of the limited exposure time, the number of observed photons decreases for distant or faint clusters, and the background becomes relatively more influential for such clusters. We adopt a detector area of 10^4 cm^2 , similar to the ROSAT telescope.

In order to mimic current X-ray telescopes, we choose spatial and energy resolutions modeled after the ROSAT HRI (David et al. 1993) and the ASCA *Solid-State Imaging Spectrometer* (SIS; Tanaka, Inoue, &

Holt 1994). Images are taken with the properties of the HRI, which has no energy resolution and a spatial resolution of a few arc seconds. We assume a Gaussian point-spread function with $4''$ width. Spectra are taken with the energy resolution of the ASCA SIS, i.e.,

$$\frac{\Delta E}{E} = 0.02 \left(\frac{E}{5.9 \text{ keV}} \right)^{-1/2}. \quad (8)$$

We do not attempt to model the complicated ASCA point-spread function in detail (Takahashi et al. 1995; Serlemitsos et al. 1995). Rather, we take it to be Gaussian with $90''$ width. Consequently, the spatial resolution of the simulated cluster spectra is much lower than that of the synthetic cluster images. We choose this procedure such as to model combined cluster analyses based on the best (i.e., most highly resolved) cluster images and spectra available today. The HRI energy band is $0.1 \leq E/\text{keV} \leq 2.4$, the SIS band is $0.3 \leq E/\text{keV} \leq 12$.

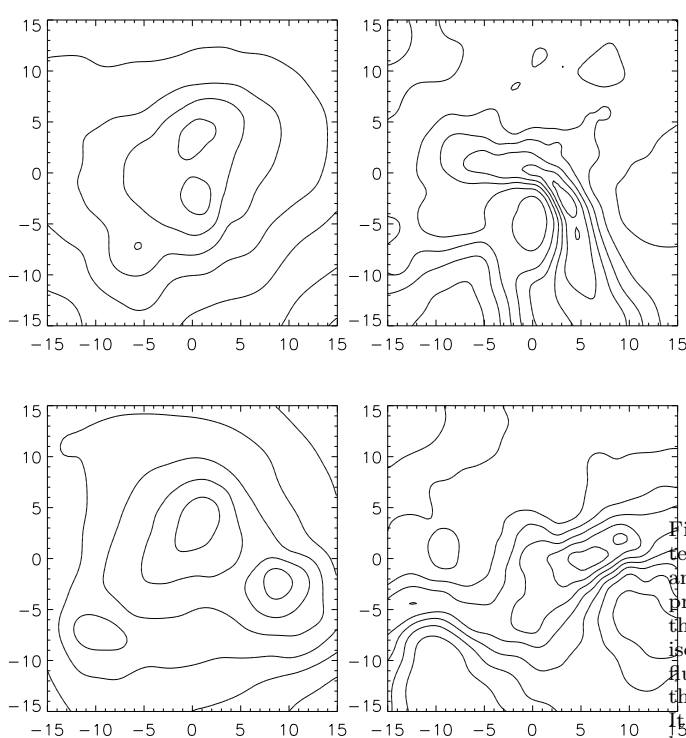


Figure 1.— Left column: Isodensity contours for a cluster which is undergoing a merging event. The upper and lower panels correspond to two different spatial projection directions. Left column: isoflux contours of the X-ray emission; right column: (emission-weighted) isotherm contours of the intracluster gas. The flux contours are logarithmically spaced by 0.5 decades, the temperature contours are linearly spaced by 2 keV. It is seen in the top right frame that the brighter clump has a bow shock, and the bottom right frame shows a shock between the merging clumps.

2.3. The Cluster Sample

The cluster sample is virtually identical to that analyzed for its lensing properties in Bartelmann et al. (1995), but it was re-simulated including gas-dynamical effects. Within r_{500} (the radius of the sphere within which the averaged cluster density is 500 times the background density), the clusters have total masses between $6 \times 10^{14} M_{\odot}$ and $4 \times 10^{15} M_{\odot}$ and line-of-sight velocity dispersions between 700 and 1200 km s^{-1} . The mass resolution is $3 \times 10^{11} M_{\odot}$ in dark matter and $1.6 \times 10^{10} M_{\odot}$ in gas, i.e. each cluster is resolved into between 2000 and 12000 particles of each species. The emission-weighted central temperatures range between 4 keV and 13 keV, respectively. Many of the clusters are quite relaxed and exhibit only small amounts of substructure. Their temperature profiles are fairly flat; the central temperatures deviate from the averaged emission-weighted temperature by less than a factor of about 1.5. The isodensity and isotemperature contours are usually almost concentric. Typically for a high- Ω_0 cosmogony, the clusters undergo strong evolution even at redshifts close to zero. However, due to our high normalization ($\sigma_8 = 1$), our galaxy clusters are not as rare as in the canonical CDM cosmogony normalized to the observed cluster

abundance (White et al. 1993) which corresponds to $\sigma_8 = 0.6$. The amount of substructure in our cluster sample should, therefore, provide a compromise between the extremes of a low-normalized $\Omega_0 = 1$ and a high-normalized $\Omega_0 = 0.3$ universe. During an epoch of merging the clusters exhibit bimodal or even more complex density structures. Isodensity and isothermality contours then deviate significantly from each other (cf. Fig. 1). The temperature maximum does not coincide with the density maximum but falls between two merging subclumps or on the bow shock of an infalling clump (Fig. 1, right column). Shocks are then abundant in the intracluster gas, and there the peak gas temperatures T_{peak} are substantially higher than the broad-band average temperatures T_{avg} .

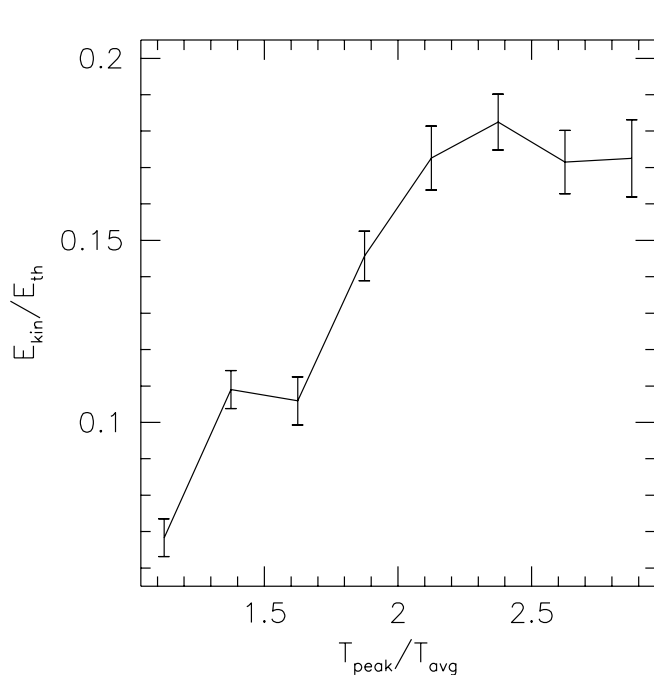


Figure 2.— Energy ratio ϵ as defined in eq. (9) as a function of the temperature excess τ (eq. (10)). Unrelaxed clusters whose kinetic energy is to a significant part in form of bulk motions of the gas also exhibit a large ratio of maximum to averaged temperature, i.e., the ratio τ is a good indicator for ongoing merging.

In Fig. 2 we plot the quantity

$$\epsilon \equiv \frac{E_{\text{kin}}}{E_{\text{th}}} \quad (9)$$

as a function of

$$\tau \equiv \frac{T_{\text{peak}}}{T_{\text{avg}}}, \quad (10)$$

where $E_{\text{kin,th}}$ are the kinetic and thermal energies of the intracluster gas, respectively. Values of ϵ close to zero indicate complete thermalization of the gas, and the influence of bulk motions increases with increasing ϵ . As can be seen in Fig. 2, those clusters which have a high τ also have high ϵ , i.e., they are not relaxed, and the kinetic energy of the gas can reach 20 per cent of the thermal energy. Navarro et al. (1995a) argued that ongoing merging is accompanied by a boost in the velocity dispersion and, therefore, the ratio $\beta_{\text{T}} \equiv \mu m_{\text{p}} \sigma_{\text{DM}}^2 / kT > 1$ may be a good indicator for merging. For similar reasons, merging also causes a boost in the peak temperature of the cluster ($\tau > 2 - 3$). However, the ratio τ is probably much more easily accessible to observation (cf. Briel & Henry 1994; Henry & Briel 1995).

3. Mass Determinations

Given the photon tables for each cluster, we determine spectral temperatures and then proceed to apply two techniques to determine their masses.

3.1. Temperature Determination

Equation (7) yields the number of photons $d\gamma(T, n_e)$ per energy interval dE of a volume element of the intracluster gas with temperature T and electron density n_e . Summing over all volume elements (grid cells) and binning the photons according to the energy resolution (8), we can compute synthetic spectra. For each cluster image, such spectra are determined within rings of width $1'$ around the X-ray centroid, taking into account that the spatial photon distribution is broadened by the PSF of the X-ray telescope.

Spectral temperatures are then found by fitting eq. (7) to the spectra. We find that the spectral temperatures are on average accurate to $\sim 10 \dots 15$ per cent. The average $1\text{-}\sigma$ error of the best-fit temperatures is ~ 20 per cent. Since X-ray cluster mass estimates are proportional to the gas temperature (see below), this scatter is directly propagated to an additional uncertainty in the cluster masses. Within the error bars, there is no systematic trend with temperature in the accuracy of the temperature determination. Note, however, that the accuracy of our temperature estimates is still idealized in so far as in the case of observed clusters the accuracy can be further reduced by imperfections in the discrimination between bremsstrahlung emission and emission in individual metal lines, which depends on, e.g., the assumptions about metal abundances in the intracluster gas.

3.2. β -fit Models

The most common technique to determine cluster masses from their X-ray emission is the β -fit method, pioneered by Cavaliere & Fusco-Femiano (1976) and widely used thereafter (e.g., Jones & Forman 1984; Henriksen & Mushotzky 1985; Edge & Stewart 1991). The photon flux is azimuthally averaged in radial bins around the observed X-ray centroid, yielding a flux profile of the cluster. The three-parameter function

$$S_X = S_0 (1 + x^2)^{-3\beta+1/2} \quad (11)$$

is then fit to the observed profile, where x is the distance from the X-ray centroid in units of a core radius r_c . The three parameters S_0 , r_c , and β are then adjusted such as to optimize the fit. β -fits obtained this way usually provide excellent fits to the X-ray emission profile, both for real and for simulated cluster emission (cf. the example profile and fit in Fig. 4).

We can ignore the weak temperature dependence $\propto T^{1/2}$ of thermal bremsstrahlung emission, because the intracluster gas is almost isothermal over the radial range of the fit. The X-ray emission is then determined by the square of the gas density, and hence the form of the fit in eq. (11) implies

$$\rho_{\text{gas}}(r) = \rho_{\text{gas},0} (1 + x^2)^{-3\beta/2}. \quad (12)$$

If the gas is in hydrostatic equilibrium in a spherically symmetric potential well produced by the dark-matter distribution, and if it is isothermal, then Euler's equation implies

$$M(r) = -\frac{r kT}{G\mu m_p} \frac{d \ln \rho_{\text{gas}}}{d \ln r}, \quad (13)$$

where G is Newton's constant, m_p is the proton mass, and

$$\mu = \frac{4}{5f + 3}, \quad \mu = 0.59 \quad \text{for} \quad f = 0.75 \quad (14)$$

is the mean molecular weight of a hydrogen-helium mixture with hydrogen fraction f (by weight). Given β and r_c from fitting the X-ray surface brightness, eqs. (12) and (13) imply

$$M(r) = \frac{3\beta r kT}{G\mu m_p} \frac{x^2}{1 + x^2}. \quad (15)$$

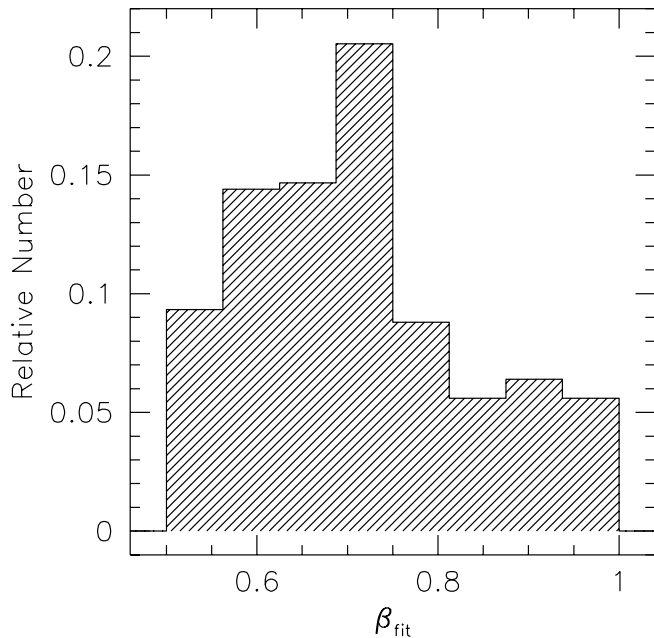


Figure 3.— Distribution of β values fit to the cluster X-ray profiles. The average is close to $\langle\beta\rangle \sim 2/3$.

Figure 3 shows a histogram of best-fit β values obtained from our cluster sample. The distribution of values obtained from our simulations compares well with observationally determined distributions (e.g., Jones & Forman 1984; Henriksen & Mushotzky 1985; Edge & Stewart 1991).

Note that eq. (15) implies the dark-matter density profile

$$\rho(r) = \rho_0 \frac{3 + x^2}{3(1 + x^2)^2}, \quad \rho_0 = \rho(0) = \frac{9\beta kT}{4\pi G\mu m_p r_c^2}. \quad (16)$$

The density profile asymptotically approaches the isothermal fall-off $\propto x^{-2}$. The density profiles of our numerically simulated clusters however are of the form recently found by Navarro, Frenk, & White (1995b),

$$\rho(y) = \frac{\rho_s}{y(1 + y)^2}, \quad (17)$$

where y is the radius in units of a scaling radius r_s . Since this profile is steeper by one power of r than the isothermal β -fit density profile, the isothermal β -fit mass profiles are flatter than the true profiles. In particular, the accuracy of β -fit mass estimates depends on radius.

For gas in hydrostatic equilibrium with the dark-matter potential which has the same temperature as the dark-matter particles,

$$kT = \mu m_p \sigma_{\parallel}^2, \quad (18)$$

where σ_{\parallel} is the line-of-sight velocity dispersion of the dark-matter particles. The physical meaning of the parameter β in hydrostatic equilibrium is

$$\beta = \frac{\mu m_p \sigma_{\parallel}^2}{kT}. \quad (19)$$

Since eq. (18) is well fulfilled in our numerical simulations, and since the simulated dark-matter density profiles asymptotically fall off $\propto r^{-3}$, we should expect to obtain $\beta \sim 1$ from fitting the X-ray profiles with the β model (11). The reason why we find systematically low β values is illustrated in Fig. 4. There, we show the same background-subtracted X-ray profile four times, each time with a different level for the adopted X-ray background which is indicated by the dotted horizontal lines. The β model is fit to the X-ray emission profile out to the radius where the profile falls below the background level. The secondary peak at $r \sim 10'$

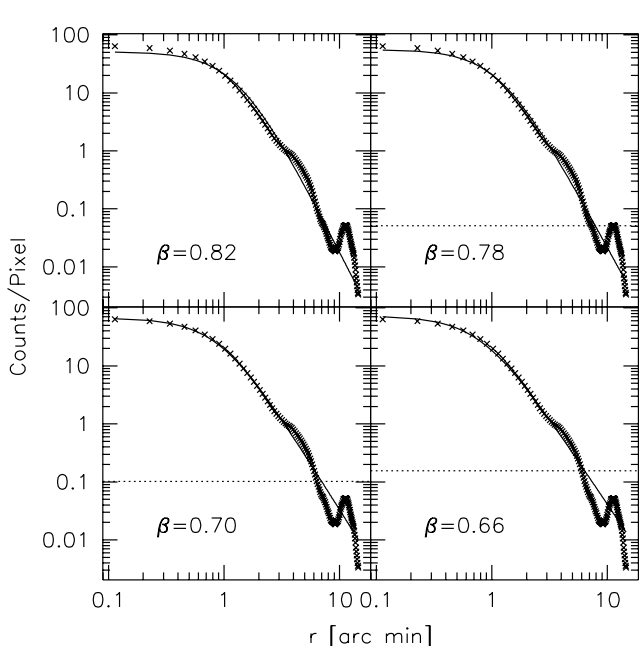


Figure 4.— The same simulated X-ray emission profile is plotted four times (crosses). The adopted X-ray background is increased from zero (top left frame) to $[1, 2, 3] \times 10^{-4} \text{ s}^{-1} \text{ arcmin}^{-2}$ (top right, bottom left, and bottom right frame, respectively) as indicated by the dotted horizontal lines. The solid lines in all frames are the β models obtained by fitting the profile out to the radius where they fall below the background. With increasing background intensity and thus decreasing radial range of the fit, β drops from 0.82 to 0.66. The secondary peak at $r \sim 10'$ is excluded from the fit.

is excluded from the fit. The solid line is the best-fit β profile obtained, and the optimal β values are given in each frame.

The figure shows that the best-fit β value decreases while the background is gradually increased. Without the background, $\beta = 0.82$ (top left frame), and when the background reaches the level of $3 \times 10^{-4} \text{ s}^{-1} \text{ arcmin}^{-2}$ adopted throughout our simulations, β drops to 0.66. Hence, the reason for the systematically low β values in our simulations is the limited range of radii accessible with X-ray observations. Where the emission reaches the background level, the profile has not yet reached its asymptotic slope.

The observed discrepancy between β_{fit} as obtained from fitting the profile (11) and β_{spec} as obtained through (19) from measuring T and σ_{\parallel} has been widely discussed in the literature (see, e.g., Sarazin 1986 for a review). Since our numerically simulated clusters satisfy $\beta_{\text{spec}} \simeq 1$, they reproduce the observed β discrepancy. Several solutions to the β problem have been suggested. Lubin & Bahcall (1993) and Bahcall & Lubin (1994) showed that the β discrepancy disappeared when they adopted the actual radial profile of the cluster galaxy distribution rather than the King profile underlying eq. (11), which is equivalent to assuming a flatter dark-matter density profile. Evrard (1990) ascribed the β discrepancy in his numerically simulated galaxy clusters to a combination of incomplete thermalization of the intracluster gas and anisotropic dark-matter velocity distributions. Navarro et al. (1995a) also found the β discrepancy in their models and concluded that (1) β_{fit} is biased low because of the limited radial range available for fitting the X-ray profile and (2) the actual slope of the dark matter profile in the relevant radial range is smaller than its asymptotic slope. Although the intracluster gas in our simulations is not completely thermalized either, this has only a weak influence on the β discrepancy because on average the kinetic energy of the gas is only ~ 10 per cent of the thermal energy (cf. Fig. 10 below). Our results therefore support the view of Navarro et al. (1995a) that the limited radial range accessible to cluster observations is sufficient to explain the β discrepancy.

Figure 4 illustrates an additional effect which can cause β fits to be systematically low. At $r \sim 4'$ in the example plotted there, there is a low hump in the profile which is due to the emission of a small infalling subclump. Despite this subclump, the cluster image looks almost spherically symmetric. Although weak, the hump in the profile flattens the best-fit β model if it is close to the background cutoff as in the case of the profile shown in Fig. 4.

3.3. Masses Based on the King Profile

We have seen that the β model yields systematically low β values because of the restricted radial range within which the fits can be done. Since we have good theoretical reasons to believe that dark-matter density profiles

asymptotically fall off $\propto r^{-3}$ (Navarro et al. 1995b; Cole & Lacey 1995), it appears preferable to base X-ray mass estimates on the assumptions that (1) the dark-matter density profile can be described by some profile $\propto r^{-3}$ for large r and (2) that the X-ray gas is in thermal and hydrostatic equilibrium with the dark-matter potential. Then, the gas density profile has the same shape as the dark-matter density profile. We should however add the cautionary note that it has not been verified yet that actual galaxy clusters follow the density profiles found numerically.

To illustrate that procedure, we choose King’s approximation to the isothermal profile (King 1966; Binney & Tremaine 1987),

$$\rho(r) = \rho_0 (1 + y^2)^{-3/2}, \quad (20)$$

where y is the distance from the X-ray centroid in units of the King radius,

$$r_K = \left(\frac{9\sigma_{\parallel}^2}{4\pi G\rho_0} \right)^{1/2}. \quad (21)$$

The integrated dark mass can then be written

$$M(r) = \frac{9kT r_K}{G \mu m_p} f(y), \quad (22)$$

$$f(y) \equiv \ln \left(y + \sqrt{1 + y^2} \right) - \frac{y}{\sqrt{1 + y^2}}.$$

We find the King radius r_K in our simulations by fitting the profile

$$S'_X = S'_0 (1 + y^2)^{-5/2} \quad (23)$$

to the simulated X-ray profiles. This is equivalent to fitting a β model under the constraint $\beta = 1$. We note that this is similar to the approach suggested by Evrard et al. (1995) which consists in constraining the value of β with scaling laws obtained from numerical simulations.

3.4. Results for Mass Estimates

We now display and summarize the results for the two different methods to estimate X-ray masses which we have applied to the numerically simulated clusters. Figure 5 shows the ratio between estimated and true cluster mass as a function of radius. The radii are scaled by the radius r_{500} within which the density contrast of the cluster relative to the background density is 500 in order to superpose the results obtained from all simulated clusters. We restrict the plots to clusters at redshifts below 0.5. The frames in the left column of Fig. 5 show results for low-redshift clusters ($0 \leq z < 0.25$), and the results for intermediate-redshift clusters ($0.25 \leq z < 0.5$) are displayed in the right column. The top frames show β -fit mass estimates, and the bottom frames show mass estimates assuming a King profile for both the dark-matter and the gas density. The error bars give the $1-\sigma$ scatter in all applicable simulations.

First, we note that there is no substantial difference between the low- and the intermediate-redshift cluster samples. The accuracy of the β -fit mass estimates depends on radius as discussed before: Since the isothermal β -fit mass profile is shallower than the true mass profile, the ratio between the estimated and the true mass increases with radius. In contrast to that, the estimates assuming the King profile are almost flat within the error bars, and over most of the range of radii accessible to X-ray observations the accuracy is significantly improved over that of the β -fit mass estimates. The slightly falling curves in the bottom left frame indicate that for the low-redshift cluster sample the King profile is slightly too steep. This is due to merging of subclumps which renders radially averaged mass profiles shallower than the King profile expected for an isolated cluster. Also note that the mass estimates from the King model are biased somewhat low. We will discuss the reason below.

Some further features of the different mass estimates are illustrated in Figs. (6) and (7). Figure 6 displays histograms for the distribution of cluster mass estimates at the maximum radius r_{obs} accessible to X-ray observations, where the surface brightness drops to the background level. The frames are arranged as in Fig. 5: The top frames show β -fit results, the bottom frames show results from the assumption of a

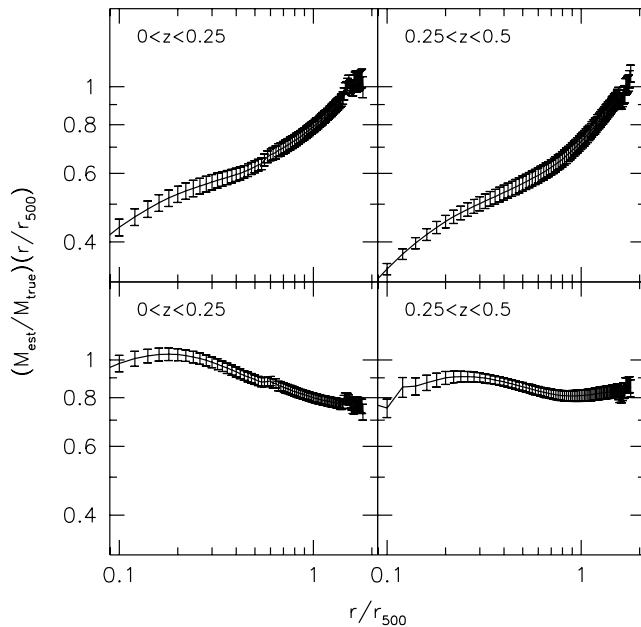


Figure 5.— Ratio between the estimated and the true cluster mass $M_{\text{est}}/M_{\text{true}}$ as a function of radius. The radii are scaled by the radius r_{500} so that the results from all clusters can be superposed. The left (right) frames are for low- (intermediate-) redshift clusters as indicated, the top (bottom) frames are for β (King-profile) fits, respectively. While the mass ratio obtained from β fits rises with r , it is almost flat for the King-profile fits. This reflects the fact that the isothermal mass profiles obtained from the β fits are shallower than the true mass profiles. Error bars indicate the $1-\sigma$ scatter over all applicable simulations.

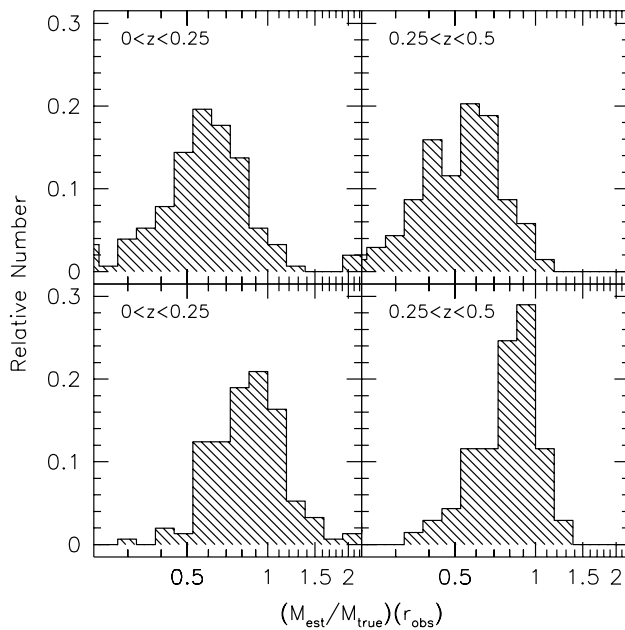


Figure 6.— Histograms for the distribution of the ratio $M_{\text{est}}/M_{\text{true}}$ at the maximum observable radius r_{obs} . The frames are arranged as in Fig. 5. The distributions of the β -fit mass estimates peak at ~ 0.6 , while the estimates from King-profile fits peak at ~ 0.9 . The scatter in the β -fit results is much larger than for the King-profile fits because of the uncertainty in the best-fit values of β .

King profile. The left and right columns displays results for low- and intermediate-redshift cluster samples, respectively.

The β -fit mass estimates are centered on $M_{\text{est}}/M_{\text{true}} \sim 0.6$, while the King-profile estimates peak at ~ 0.9 . Also, the width of the distributions is reduced by fitting the King profile because the scatter in the best-fit β values is removed.

To further highlight the influence of the systematic bias in the β values on the accuracy of the mass estimates, Fig. 7 displays the ratio $M_{\text{est}}/M_{\text{true}}$ at the observable radius r_{obs} as a function of β .

As expected from eq. (15), Fig. 7 shows a roughly linear relation between the accuracy of the mass

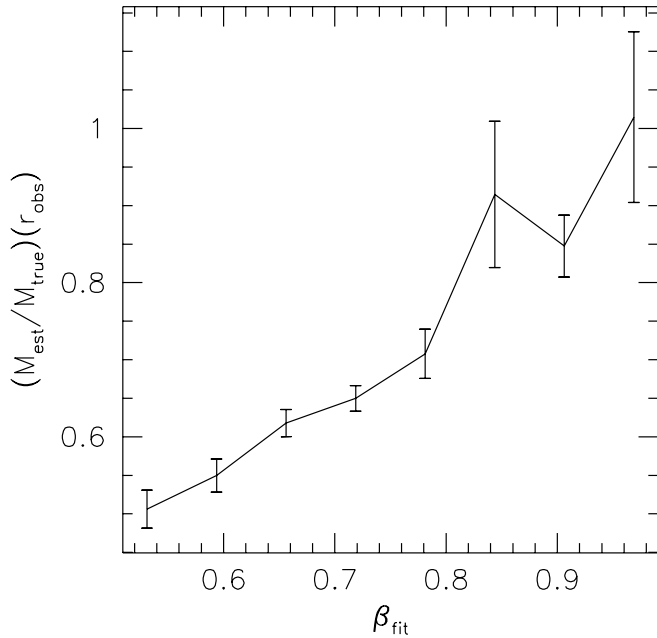


Figure 7.— Ratio $M_{\text{est}}/M_{\text{true}}$ from β fits at the radius r_{obs} as a function of β . The curve shows a roughly linear relation between the accuracy of the mass estimates and β . For $\beta \sim 1$, the masses estimates are accurate, and they drop to ~ 60 per cent of the true mass for the average value $\beta \sim 2/3$.

estimates and β . For clusters with $\beta \sim 1$, the mass estimates are almost exact, and they drop in proportion to β . At the average $\beta \sim 2/3$, the estimated mass at r_{obs} is ~ 60 per cent of the true mass.

As mentioned before, also the mass estimates based on the King-profile fits are systematically low by ~ 10 per cent (e.g., the histograms in the bottom frames of Fig. 6 peak at $M_{\text{est}}/M_{\text{true}} \sim 0.9$). The reason for that is illustrated in Fig. 8, where we plot as the solid line the accuracy of the mass estimates from the King profile in dependence on the ratio between the kinetic and the thermal energy of the gas. The dotted line shows the mass estimates multiplied by the factor $1 + E_{\text{kin}}/E_{\text{th}}$.

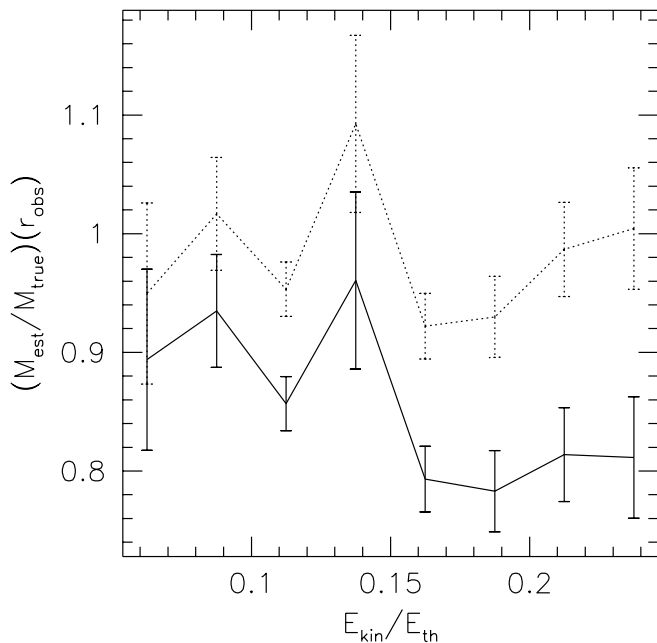


Figure 8.— Solid line: Ratio $M_{\text{est}}/M_{\text{true}}$ obtained from King-profile fits at the radius r_{obs} as a function of the ratio $E_{\text{kin}}/E_{\text{th}}$ between the kinetic and the thermal energy of the cluster gas. The dotted line shows the same results multiplied by the factor $1 + E_{\text{kin}}/E_{\text{th}}$ by which the gas temperature should be higher if the gas was fully thermalized. The figure shows that mass estimates are biased low in the presence of bulk flows in the cluster gas because then the gas temperature is systematically low. The corrected curve shows that the mass estimates are accurate to within the error bars if the cluster gas is completely thermalized.

The figure shows that the accuracy of the mass estimates decreases with increasing fraction of kinetic

relative to thermal gas energy. This fraction indicates the presence of bulk flows in the gas. In the presence of bulk flows, the gas is not fully thermalized, and therefore the gas temperature is lower than it should be if pressure equilibrium was maintained by thermal gas pressure only. Low temperature biases the mass estimates low. If the gas can be considered in virial equilibrium with the cluster potential but not yet in thermal equilibrium, this bias should amount to the ratio between the thermal energy and the sum of thermal and kinetic energy because the mass is proportional to the gas temperature. Therefore, if we multiply the mass estimates by the factor $1 + E_{\text{kin}}/E_{\text{th}}$, we correct for the low temperature. Although the scatter is large, the corrected (dotted) curve in Fig. 8 shows that the corrected mass estimates are accurate to within the error bars.

4. Properties of Lensing X-ray Clusters

4.1. Arc Cross Sections

Our method to investigate the arc-formation statistics of the numerical cluster models was described in detail by Bartelmann & Weiss (1994). We will therefore keep the present description brief and refer the reader to that paper for further information. For general information on gravitational lensing, see Schneider, Ehlers, & Falco (1992) and references therein.

The numerical cluster models yield the spatial coordinates and velocities of discrete particles with equal mass. In order to use them for gravitational lensing, we need to compute the surface mass density distribution of each cluster model in each of the three independent directions of projection. The mass density is first determined on a three-dimensional grid according to eq. (1) and subsequently smoothed with a Gaussian filter function. The grid resolution and the width of the Gaussian are adapted to the numerical resolution of the code in order not to lose spatial resolution by the smoothing of the density field. The smoothed density field is then projected onto the three sides of the computation volume to obtain three surface-density fields for each cluster.

The physical surface mass density fields are then scaled by the critical surface mass density for lensing, which apart from the cosmological parameters depends on the cluster- and source redshifts. We keep the redshift for all sources fixed at $z_s = 1$, and the cluster redshifts vary between $0 \leq z_c \leq 1$. This finally yields three two-dimensional convergence fields $\kappa(\mathbf{x})$ at the two-dimensional position \mathbf{x} for each cluster model. From $\kappa(\mathbf{x})$, all quantities determining the local lens mapping, i.e., the deflection angle and its spatial derivatives, can be computed. We determine the lens properties of the clusters on grids with an angular resolution of $0''.3$ in the lens plane in order to ensure that lensed images be properly resolved.

Sources are then distributed on a regular grid in the source plane. The resolution of this source grid can be kept low close to the field boundaries because there no large arcs occur. Close to the caustics of the clusters, where the large arcs are formed, the source-grid resolution is increased with the increasing strength of the lens. For our later purpose of statistics, sources are weighted with the inverse resolution of the grid on which they are placed. The sources are taken to be intrinsically randomly oriented ellipses with their axis ratios drawn randomly from the interval $[0.5, 1]$, and their axes determined such that their area equals that of circles with radius $0''.5$. Although this choice of source properties appears fairly simple, it should not affect the arc statistics because the latter mainly reflects the local properties of the lens mapping, which are independent of the particular choice of source sizes or the ellipticity distribution.

The sources are then viewed through the cluster lenses. All images are then classified in the way detailed by Bartelmann & Weiss (1994). Among other things, the classification yields for each image its length L and its width W . In total, we classify the images of about 78,000 sources lensed by 80 cluster models.

Knowing the area covered by the cluster fields, and having determined the frequency of occurrence of image properties such as a given length and width, we can compute cross sections for the formation of images with such properties. This procedure yields tables σ_{ijk} of cross sections in units of $(h^{-1} \text{ Mpc})^2$, one each for cluster model i , projected along the spatial direction j , at time or redshift k . We then interpolate these cross-section tables between the discrete redshifts to obtain cross sections $\sigma_{ij}(z)$ as smooth functions of cluster redshift z for each cluster i and each projection direction j , and finally average these cross sections

over all i and j . The result is the average cross section per cluster $\langle\sigma\rangle(z)$ as a function of redshift. Examples for the cross sections $\langle\sigma\rangle(z)$ can be found in Bartelmann et al. (1995).

4.2. Optical-Depth Weighted Averages

We want to study properties of such X-ray clusters which are selected for their lensing effects, more specifically for their ability to produce arcs. We therefore need to introduce an averaging procedure which weights the cluster properties under consideration with the arc optical depth contributed by the individual clusters. A straightforward way to do so (cf. Bartelmann 1995) is to define the optical-depth weighted average of a quantity by

$$\bar{Q}_{ij} = \frac{1}{\tau_{ij}(z_s)} \int_0^{z_s} dz \frac{d\tau_{ij}(z)}{dz} Q_{ij}(z), \quad (24)$$

where the model indices i and j indicate that the averages are to be taken for each cluster model and each projection direction separately. The optical depth $\tau_{ij}(z_s)$ is the optical depth for lensing of sources at redshift z_s , contributed by the cluster model specified by (i, j) , which is defined as the probability with which a source at redshift z_s is imaged as an arc with certain specified properties. It is given as an integral over lens redshift of the cross section $\sigma_{ij}(z)$ of the given cluster model, weighted by the proper volume and divided by the area of the source sphere,

$$\tau_{ij}(z_s) = \frac{1}{4\pi D_s^2} \int_0^{z_s} dz \left| \frac{dV(z)}{dz} \right| n_0 (1+z)^3 \sigma_{ij}(z). \quad (25)$$

D_s is the angular-diameter distance to the source, $dV(z)$ is the proper volume element at redshift z , n_0 is the comoving cluster density, and the factor $(1+z)^3$ accounts for the cosmic expansion. The quantity \bar{Q} averaged over the entire cluster sample is finally given by

$$\bar{Q} = \frac{1}{\tau(z_s)} \sum_{ij} \tau_{ij}(z_s) \bar{Q}_{ij}. \quad (26)$$

Of course, the results depend on the arc properties chosen. In the following, we choose the arc length-to-width ratio $L/W \geq 10$ to perform the averages (24) and (26), i.e., we select for giant arcs.

4.3. Arc-Cluster Properties

We start by comparing different estimates of the total cluster mass within the arc radius. We show in Fig. 9 the distribution of the true cluster mass (i.e., the total mass of all cluster particles) in panel (a) together with the distributions of mass estimates derived from lensing [panel (b)], and from β - and King-profile fits to the cluster X-ray emission [panels (c) and (d), respectively].

The lensing mass estimate is given by the average convergence $\bar{\kappa}$ within circles traced by the arcs, multiplied by the area enclosed by the circles and the critical surface mass density Σ_{cr} . The lensing mass estimate is therefore the projected cluster mass within a cylinder around the line-of-sight with radius equal to the distance between the arc and the cluster center. For spherically symmetric clusters, $\bar{\kappa} = 1$ by definition of the tangential critical curve. For asymmetric clusters, $\bar{\kappa}$ is systematically below unity (Bartelmann 1995), hence the simple mass estimate based on $\bar{\kappa} = 1$ would overestimate the projected cluster mass. The true $\bar{\kappa}$ which we adopt here is not directly accessible through observations of strong lensing, but the success of cluster mass models reproducing observed arcs and multiple images indicates that reliable estimates of $\bar{\kappa}$ can be given in practice.

A comparison between panels (a) and (b) of Fig. 9 shows that the distributions of the true dark mass and the lensing mass agree very well although the lensing mass is projected along the line of sight. If lensing clusters were preferentially elongated along the line-of-sight such as to increase their surface mass density, the lensing mass would be significantly larger than the true mass. The fact that this is not the case demonstrates that such a selection effect on arc clusters is at least statistically unimportant. The distribution of the β -fit mass estimates (panel c) peaks at $\sim 1.5 \times 10^{14} M_\odot$, while the distribution of true cluster masses peaks at about 2.5 times this value. This reflects the fact that best-fit β values are systematically too low especially at the rather small radii where large arcs appear in clusters, and that the isothermal dark-mass profiles are shallower than the true cluster profiles. The mass estimates based on King-profile fits shown in panel (d)

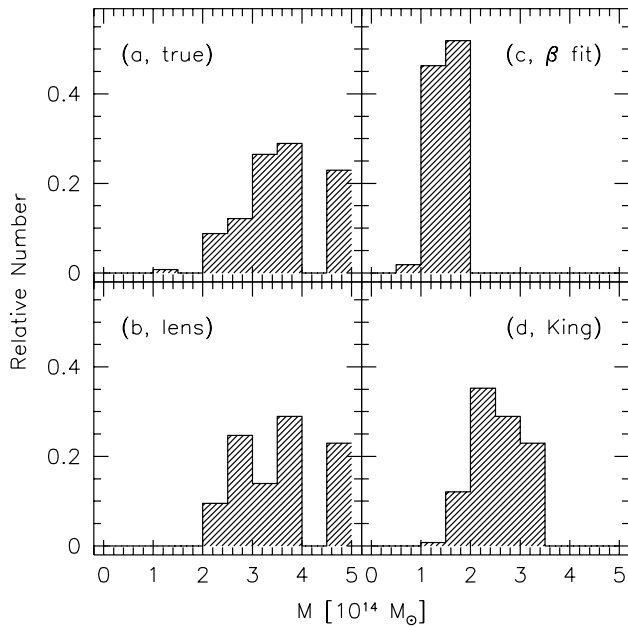


Figure 9.— Distributions of cluster masses in $10^{14} M_{\odot}$ and different mass estimates at the arc radius. (a) true cluster mass; (b) lensing mass, i.e., projected mass; (c) β -fit mass estimates; (d) mass estimates from King-profile fits. The comparison between frames (a) and (b) show that the distributions of lensing- and true masses are almost identical, indicating that projection effects of lensing clusters are statistically unimportant. The β fit mass estimates are systematically low by a factor of $\sim 2 - 3$, while the mass estimates from the King-profile fits are low by ~ 20 per cent.

are significantly better than the β -fit masses, but they are still systematically smaller than the true masses by a factor of ~ 0.8 .

We have seen above that the low-biased β -fit mass estimates are mainly caused by the fact that the β fits to the X-ray emission profiles are restricted to a range of radii within which the profiles have not reached their asymptotic fall-off yet. King-profile fits are biased low mainly if the cluster gas is not yet fully thermalized, in which case the X-ray temperatures are lower than in equilibrium. To emphasize this point, we compare in Fig. 10 the distribution of the ratio of kinetic and thermal energy of the X-ray gas for arc clusters (panel a) and for the entire cluster sample (panel b).

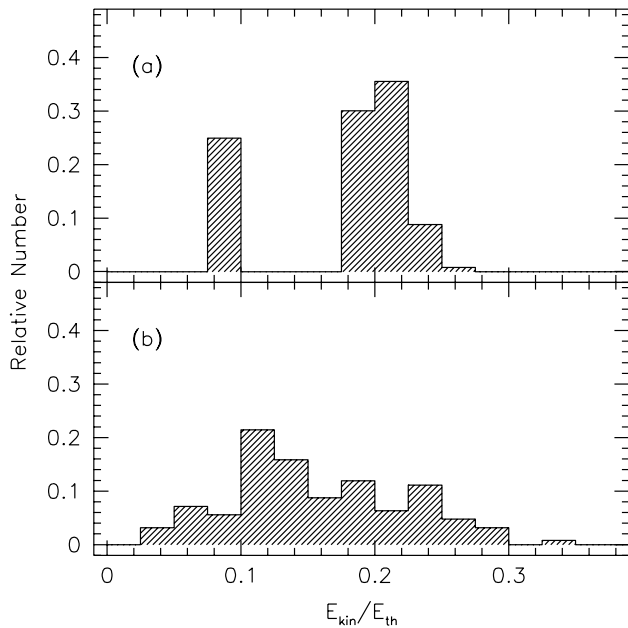


Figure 10.— Distribution of the ratio between kinetic and thermal energy of the intracluster gas for arc clusters (panel a) and for the entire cluster sample (panel b). On average, the arc clusters are less thermalized, i.e. for them a larger fraction of the energy of the gas is in bulk flows.

Figure 10 shows that the two distributions are significantly different. The significance level of a Kolmogorov-Smirnov test for a difference between the two distributions is 97 per cent. On average, the fraction of non-thermalized energy of the intracluster gas is higher in arc clusters than in the entire cluster sample, and the distribution of $E_{\text{kin}}/E_{\text{th}}$ peaks at ~ 0.2 for arc clusters. The X-ray gas temperatures in arc clusters, and hence their King-profile mass estimates, are thus too low by ~ 20 per cent on average, which is reflected by the histograms in panels (a) and (d) of Fig. 9. The higher-than-average fraction of kinetic relative to thermal energy indicates that bulk flows are prevalent in arc clusters. This corresponds to the earlier finding (Bartelmann et al. 1995) that substructure in clusters significantly increases their ability to form arcs because they have a stronger tidal field than spherically symmetric clusters and they produce caustic curves with a larger number of cusp points. Substructure indicates ongoing merger events, and during merger events the gas of the merging cluster subclumps is not in thermal equilibrium.

If such clusters which have not yet reached their equilibrium state are preferentially selected by strong-lensing events, we may suspect that arc clusters are not necessarily those clusters with the highest X-ray luminosities. The equilibrium luminosity of a cluster is determined by the square of the gas density in the cluster core. While clusters are still in the process of formation or merging from subclumps, their X-ray luminosity should be lower than after virialization. We therefore investigate the contribution of clusters to the arc optical depth as a function of their X-ray luminosity $d\tau/dL$. The results are shown in Fig. 11. There, we plot in panel (b) the differential optical depth contributed by all clusters with luminosity within dL of L , and in panel (a) the same quantity divided by the number of clusters in the corresponding luminosity interval. Panel (a) of Fig. 11 therefore shows the contribution to the optical depth per cluster.

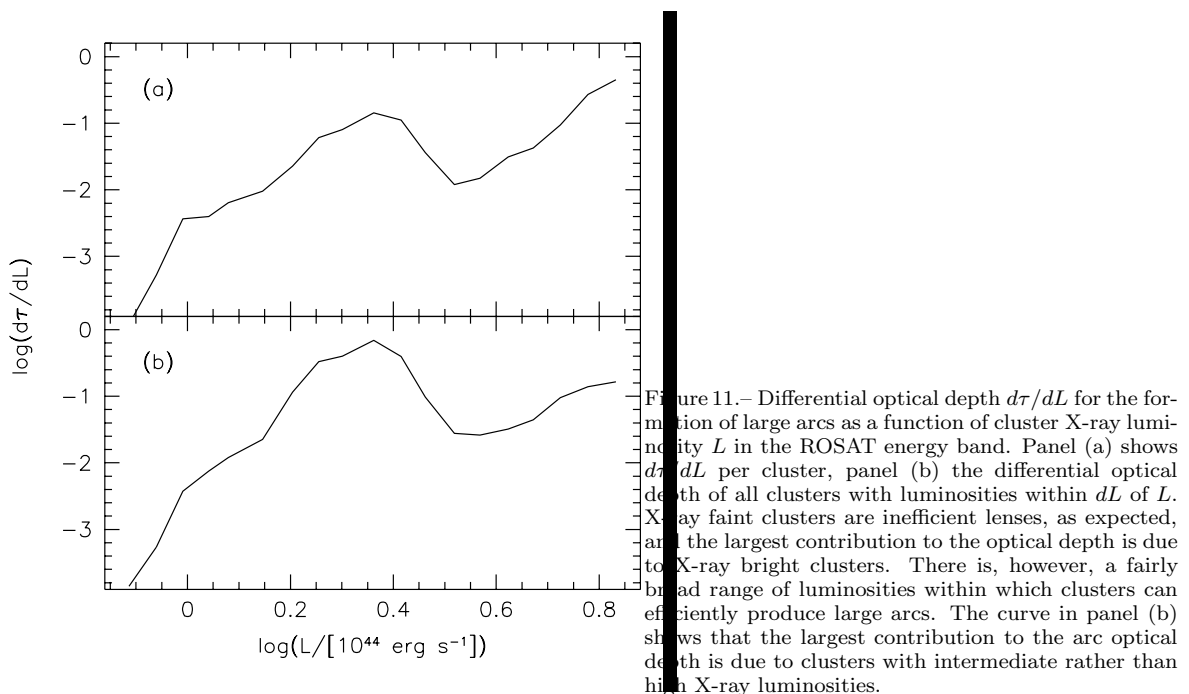


Figure 11.— Differential optical depth $d\tau/dL$ for the formation of large arcs as a function of cluster X-ray luminosity L in the ROSAT energy band. Panel (a) shows $d\tau/dL$ per cluster, panel (b) the differential optical depth of all clusters with luminosities within dL of L . X-ray faint clusters are inefficient lenses, as expected, and the largest contribution to the optical depth is due to X-ray bright clusters. There is, however, a fairly broad range of luminosities within which clusters can efficiently produce large arcs. The curve in panel (b) shows that the largest contribution to the arc optical depth is due to clusters with intermediate rather than high X-ray luminosities.

For low X-ray luminosities, the differential optical depth drops to zero, as expected. Clusters which are not bright X-ray sources are not massive or not concentrated enough in order to produce large arcs. The brightest X-ray clusters also contribute most to the arc optical depth, as seen in panel (b) of Fig. 11. There is, however, a fairly broad range of cluster luminosities within which the contribution to the optical depth per cluster is high, indicating that there is a substantial contribution to the arc optical depth from clusters with intermediate luminosities. If we consider cluster samples rather than individual clusters, as in panel (b) of Fig. 11, it turns out that clusters with intermediate X-ray luminosities, $1 \times 10^{44} \lesssim L/(\text{erg s}^{-1}) \lesssim 3 \times 10^{44}$, contribute the bulk of the arc optical depth. The shape of the curves in Fig. 11 remains the same if we split the cluster sample in halves and plot $d\tau/dL$ separately for each half. This indicates that the behaviour of the curves is not due to noise.

The form of the curves in Fig. 11 can be qualitatively understood by the following argument. Clusters with very high mass and therefore high X-ray luminosity are efficient lenses with or without substructure. Clusters with intermediate masses or luminosities are efficient lenses only if they are substructured. The optical depth is therefore composed of two contributions, one peaked contribution from intermediate-mass clusters with substructure, and one monotonically increasing contribution from high-mass clusters regardless of whether they are substructured. Intermediate-mass clusters should be most efficient lenses if and when they are in the process of formation around the redshift where the critical surface-mass density is lowest, i.e., at a redshift which is geometrically favored. For sources at $z_s = 1$ which we assume throughout, $(d \ln \tau / dz)(z)$ sharply peaks at $z \sim 0.3$ and drops to half its peak value at $z \sim 0.25$ and $z \sim 0.4$ (Bartelmann et al. 1995). Intermediate-mass clusters forming in the redshift interval $0.25 \lesssim z_f \lesssim 0.4$ should therefore contribute significantly to the optical depth because of their substructure. The formation redshift of clusters is given as a function of cluster mass by

$$z_f = \left(\frac{M}{M_*} \right)^{-1/2} \quad (27)$$

(White 1994), where M_* is the nonlinear mass today,

$$M_* = 6.3 \times 10^{13} M_\odot \sigma_8 \Omega_0^{-0.7} \quad (28)$$

(White et al. 1993). The equilibrium X-ray luminosity scales with mass as

$$L = 3 \times 10^{44} \left(\frac{M}{10^{15} M_\odot} \right)^{4/3} \left(\frac{\Omega_b}{0.05} \right)^2 \quad (29)$$

(Navarro et al. 1995a). These relations allow to translate the redshift interval $0.25 \lesssim z_f \lesssim 0.4$ to the luminosity interval $1 \times 10^{44} \lesssim L / (10^{44} \text{ erg s}^{-1}) \lesssim 3 \times 10^{44}$, which corresponds well to the luminosity range of the peaks in Fig. 11. The maximum of the curves should be reached for $z_f \sim 0.3$, corresponding to $L \sim 1.9 \times 10^{44} \text{ erg s}^{-1}$, which agrees well with the actual location of the peaks.

We can therefore conclude not only that the intrinsically brightest clusters are efficient lenses, but also that there is a fairly broad range of intermediate X-ray luminosities for which the contribution to the optical depth reaches a maximum. This range is due to clusters which form at redshifts for which the geometrical lens efficiency is highest, because while they form their substructure increases the optical depth to lensing. Only for low intrinsic luminosities does the differential optical depth fall off. Figure 11 therefore demonstrates that not the most luminous clusters are selected by lensing, but the dynamically most active ones.

4.4. Lensing Temperatures

The presence of arcs in clusters imposes a constraint on the projected cluster mass inside a cylinder with radius equal to the distance between the arc and the cluster center. This mass constraint can be converted to a temperature estimate. It was first pointed out by Miralda-Escudé & Babul (1995) that in two clusters for which X-ray and lensing data were available the temperature required to explain the lens effect is higher than the measured X-ray temperature by a substantial amount.

We apply a comparable analysis to our numerically simulated clusters here. This proceeds as follows. We fit β models to the X-ray surface-brightness profile of the clusters and obtain best-fit values for β and the core radius r_c . Assuming that the gas is isothermal, we obtain the cluster mass profile (15). Projecting this along the line of sight, we obtain

$$M_{\parallel}(r) = \frac{3\pi \beta k T r_c}{2 G \mu m_p} \frac{x^2}{\sqrt{1+x^2}}. \quad (30)$$

For the projected mass inside the arc radius we take the lensing mass as determined before. If we assumed spherical symmetry instead, the lensing mass estimate would systematically be biased high, as mentioned before. Hence we get from eq. (30)

$$k T_{\text{lens}} = \frac{2 G \mu m_p M_{\text{lens}}}{3 \pi \beta r_c} \frac{\sqrt{1+x^2}}{x^2}. \quad (31)$$

The equation shows that kT_{lens} is proportional to β^{-1} . A flatter gas profile needs to be hotter for fixed dark binding mass. The lensing temperature should therefore straightforwardly reflect the β discrepancy. Since $\beta \sim 2/3$ on average, the lensing temperatures are expected to be too high by a factor of ~ 1.5 on average. We show in Fig. 12 the distribution of the ratio between the lensing temperature and the spectral X-ray temperature of the intracluster gas.

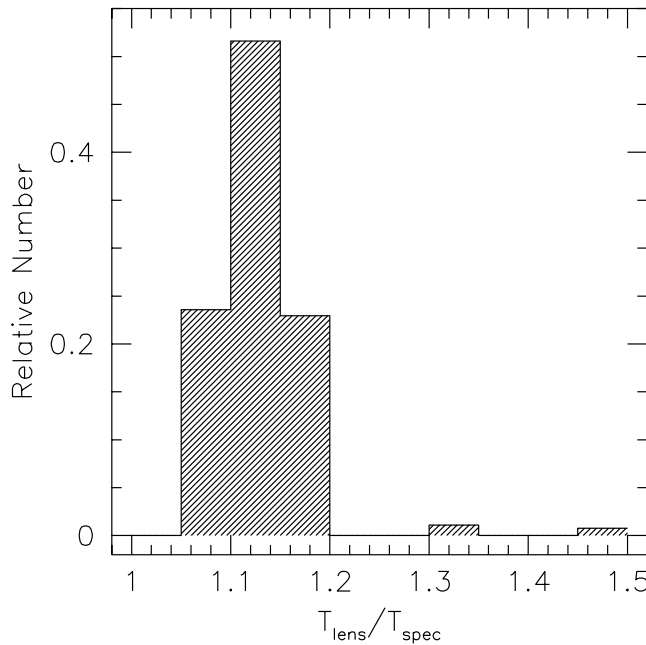


Figure 12.— Distribution of the ratio between lensing temperature T_{lens} and X-ray spectral temperature T_{spec} . The distribution peaks at ~ 1.15 , showing that on average the lensing temperature well reflects the temperature of the cluster gas with only a weak bias towards higher values of T_{lens} .

Contrary to this expectation, the lensing temperature is higher than the spectral temperature by only ~ 15 per cent. This result must, however, be interpreted with caution. Equation (16) shows that the dark-matter density profile derived from isothermal β fits falls off $\propto r^{-2}$ for large r , while the true density profile asymptotically follows r^{-3} . When projected along the line of sight, the shallower density profile contributes much more mass from large radii than the steeper profile. The flatter the profile is, the less projected mass is concentrated in the cluster center, and if there is less mass in the center, the central gas temperature can be lower. Clearly, the density profile (16) must cut off or steepen at some large radius beyond which the assumption of isothermality breaks down. In that case, M_{\parallel} would be smaller than expected from (30), hence kT_{lens} would be larger. An ambiguity then arises as to where and how the isothermal mass profile should be cut off. Thus there are two competing effects: (1) the low bias of the β values tends to increase T_{lens} , while (2) the projection along the line-of-sight of the flat isothermal mass profile tends decrease T_{lens} . Figure 12 demonstrates that the systematically low β values are almost compensated by the projection of the isothermal mass profile along the line-of-sight. We can therefore conclude that on average, the effect demonstrated by Miralda-Escudé & Babul (1995) does not occur in our sample, or in other words that for an average cluster the lensing temperature should well reflect the X-ray temperature although being somewhat too high.

However, we can identify several clusters in our sample for which kT_{lens} is higher by up to a factor two than the X-ray temperature. Given the potential importance of this discrepancy, these clusters deserve closer inspection.

We plot in Fig. 13 the distribution of radial velocities of dark cluster particles in a cylinder of $1 h^{-1}$ Mpc radius around the line-of-sight towards the three cluster models which show the largest discrepancy between T_{lens} and the X-ray spectral temperature T_{spec} .

The curves in Fig. 13 show that the radial velocity distributions for these three clusters have secondary peaks or are bimodal. This indicates infall of cluster subclumps along the line-of-sight. In these cases, the matter density of all cluster clumps projected along the line-of-sight is larger than expected in a spherically

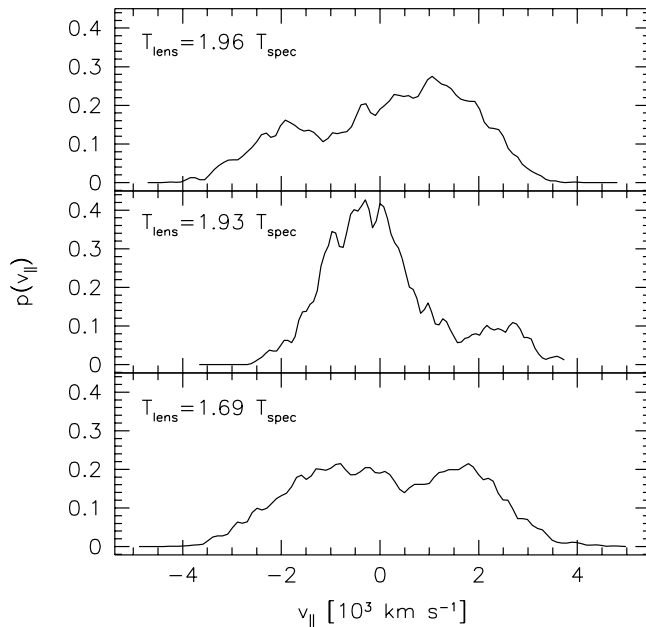


Figure 13.— Distribution of radial velocities of dark cluster particles for the three numerical cluster models in our sample which show the largest discrepancies between T_{lens} and T_{spec} . The distributions are centered, and v_{\parallel} is given in 10^3 km s^{-1} . All three distributions have secondary peaks or are bimodal, indicating infall along the line-of-sight.

symmetric model, and at the same time the X-ray temperature and luminosity are lower than expected if the total cluster matter was spherically symmetric. Therefore, although statistically unimportant, projection effects do play a role in some individual clusters for which the lensing- and X-ray temperatures are found to be discrepant.

To clarify this further, we plot in Fig. 14 the relation between the line-of-sight velocity dispersion σ_{\parallel} , divided by the average velocity dispersion $\langle\sigma\rangle$, and the ratio between the lensing- and X-ray temperatures $T_{\text{lens}}/T_{\text{spec}}$. For clusters with $\sigma_{\parallel}/\langle\sigma\rangle > 1$, the line-of-sight points along a direction into which the velocity ellipsoid of the dark cluster particles is elongated.

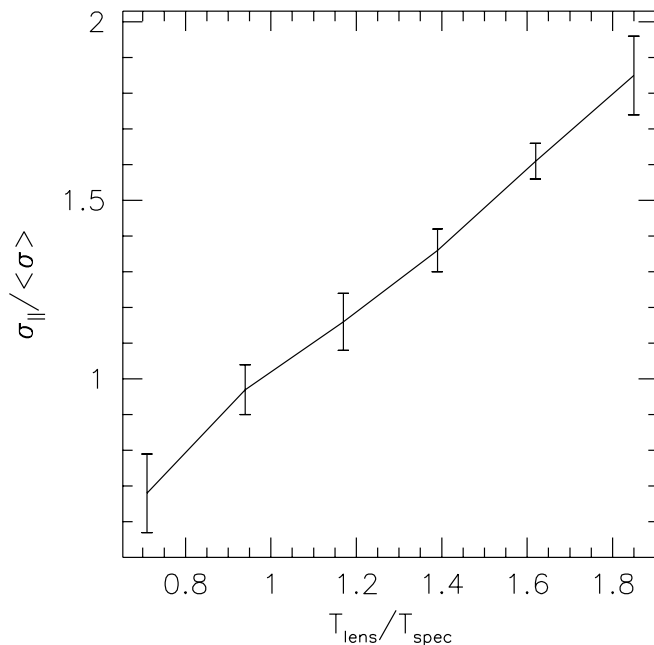


Figure 14.— Relation between the velocity dispersion along the line-of-sight σ_{\parallel} , in units of the average velocity dispersion $\langle\sigma\rangle$, and the ratio between lensing temperature T_{lens} and X-ray spectral temperature T_{spec} . Clusters whose velocity ellipsoid is elongated along the line-of-sight show a large discrepancy between lensing- and spectral temperature, indicating that this temperature discrepancy can be attributed to projection effects.

Figure 14 shows that there is an evident and strong correlation between the velocity dispersion along the line-of-sight and the lensing temperature, confirming that high values of T_{lens} relative to T_{spec} occur in such clusters which exhibit structure along the line-of-sight. The clusters analyzed by Miralda-Escudé & Babul (1995) indeed show structure in velocity space or indications of ongoing merging (Teague, Carter, & Gray 1990; Markevitch et al. 1996; Daines et al. 1996), in agreement with our findings.

5. Summary and Discussion

We have performed gas-dynamical simulations of galaxy clusters in order to compare their X-ray emission with their strong-lensing properties. The simulations were done within the CDM cosmogony. The density-perturbation power spectrum was normalized to $\sigma_8 = 1$, and the cosmological parameters $\Omega_0 = 1$, $\Lambda_0 = 0$, and $H_0 = 50 \text{ km s}^{-1} \text{ Mpc}^{-1}$ were adopted. The baryon fraction was chosen to be $\Omega_b = 0.05$. Clusters were identified in a large simulation volume and later re-simulated at much increased spatial resolution, taking the tidal effects of surrounding matter into account. We selected a sample of thirteen clusters with masses $6 \times 10^{14} \leq M_{500}/M_\odot \leq 4 \times 10^{15}$ and examined them at redshifts between zero and unity.

We calculated the X-ray emission of the cluster gas due to thermal bremsstrahlung and analyzed it imitating the imaging and spectral properties of current X-ray telescopes. Images were taken with the spatial resolution of the ROSAT HRI, and spectra were taken with the spatial and spectral resolution of the ASCA SIS. All X-ray analyses were done after discretizing the X-ray emission into photons and after adding background noise. In particular, we derived the temperature of the intracluster gas by fitting the thermal bremsstrahlung spectrum to the synthetic cluster spectra, rather than taking the temperature as given from the numerical simulations. The temperature determination was accurate to ~ 15 per cent on average. There is no systematic trend with temperature in the accuracy of the temperature determination. A total of 378 cluster images were analyzed.

We then derived mass estimates for the X-ray clusters. The first and most widely used technique to do so is to fit the β model to the azimuthally averaged cluster emission profiles. We find that the best-fitting β values are $\sim 2/3$ on average, however with a fairly large scatter. Values of $\beta \sim 1$ are expected because the cluster gas in our simulations is in equilibrium with the dark-matter particles of the clusters within the radial range where the fits can be done. Reducing the background yields significantly higher β values. This is in agreement with the earlier finding by Navarro et al. (1995a) that the systematically low β values are due to the rather limited range of radii accessible through X-ray observations. Where the X-ray emission falls below the background, the emission profiles usually have not reached their asymptotic slopes yet, and hence the best-fit β values are systematic underestimates.

The density profiles of the clusters in our simulations are well reproduced by the profile found recently by Navarro et al. (1995b), which falls off $\propto r^{-3}$ asymptotically and approaches the center $\propto r^{-1}$. Isothermal mass profiles with a flat core derived from β fits are therefore too shallow in the outer and inner parts of the clusters. Hence the accuracy of the β -fit mass estimates changes with radius. At the maximum radius accessible to X-ray observations, where the X-ray emission profile falls below the X-ray background, the β -fit masses reach ~ 60 per cent of the true mass for the average value $\beta \sim 2/3$.

Since β turned out to be systematically too low, we investigated fitting King profiles to the cluster emission rather than β models. This is equivalent to fitting the profiles constraining β to unity. Over the relevant range of radii, the density profile of the dark matter in the numerically simulated clusters can well be described by a King profile, except at the very center. It turns out that the resulting mass estimates are substantially more accurate than the β -fit mass estimates despite the reduced degree of freedom. Yet, the mass estimates are systematically low by $\sim 10 \dots 20$ per cent. We find that this remaining bias is due to bulk flows in the intracluster gas. Bulk flows indicate that the gas is not fully thermalized, so that the gas temperature is lower than it should be if the gas was completely thermalized. Observationally, they may be detectable by peaks in the temperature distribution of X-ray clusters.

We then investigated the properties of such X-ray clusters which are able to produce large arcs. We weighted cluster properties such as their mass and the relative kinetic energy of the cluster gas with the optical depth to the formation of large arcs. The distribution of lensing mass estimates relative to the distribution of true cluster masses shows that projection effects are statistically unimportant in a sample of

clusters. It is however crucial not to estimate lensing masses based on the assumption of axially symmetric lenses because in that case the lensing mass estimates are substantially too high. β -fit estimates of the cluster mass inside the arc radius are systematically lower by a factor of 1.5...2 than the true cluster masses, reflecting again the facts that (1) best-fit β values are systematically too low and (2) the isothermal β -fit mass profile is flatter than the true density profile. The mass estimates based on the King profile are significantly more accurate, although still biased low by ~ 20 per cent.

The reason for this latter bias is that the fraction of non-thermalized, kinetic energy in the intracluster gas is significantly higher in the arc clusters than in the entire cluster sample. In most arc clusters, the kinetic energy of the gas reaches ~ 20 per cent of the thermal energy, indicating that the gas temperature is only ~ 80 per cent of what it should be if the intracluster gas was completely thermalized. The X-ray temperature in lensing clusters is therefore systematically too low. This reiterates the point that strong lensing selects such clusters which show substructure. Ongoing merging of substructure gives rise to bulk flows in the intracluster gas. We also show that the bulk of the optical depth for large arcs is contributed by clusters with intermediate rather than high X-ray luminosity.

Finally, we perform an analysis similar to that done by Miralda-Escudé & Babul (1995), where they compared the cluster temperature demanded by the presence of large arcs on the basis of hydrostatic equilibrium to the measured X-ray temperature and found that for two of the three clusters they studied the lensing temperature was higher by a factor of ~ 2 than the X-ray temperature. On average, we find that the lensing temperature in our clusters well reproduces the X-ray spectral temperature with only a small high bias of ~ 15 per cent. There are, however, clusters in our sample for which the lensing temperature is indeed higher by about a factor of two than the X-ray temperature. We find that those particular clusters show structure in velocity space, indicating ongoing merging along the line-of-sight. This gives rise to projection effects which increase the lensing mass and simultaneously reduce the X-ray mass.

We can therefore summarize our major findings in the following way.

1. The β model yields systematically low cluster mass estimates because within the limited radial range accessible to X-ray observations the profile is usually shallower than it is asymptotically.
2. Fitting a King-profile to the X-ray emission substantially improves the mass estimates. These are still systematically too low by ~ 10 per cent on average.
3. The presence of bulk flows in the intracluster gas reduces the X-ray temperature by an amount proportional to the fraction of kinetic energy in the bulk flows. This accounts for the systematic bias remaining in the King-profile mass estimates. Bulk flows are accompanied by shocks in the intracluster gas which lead to significant local peaks in the temperature distribution of the clusters.
4. Strong lensing selects clusters which are dynamically more active than the average. The distribution of the relative kinetic energy of the intracluster gas peaks at significantly higher values in arc clusters compared to the entire cluster sample, indicating the prevalence of bulk flows and thus of ongoing merging in arc clusters.
5. The bulk of the optical depth to strong lensing is contributed by clusters with intermediate rather than high X-ray luminosities.
6. Cluster temperatures derived from the presence of large arcs in clusters are generally in good agreement with the X-ray temperatures of the same clusters. Such clusters where the lensing temperature is significantly higher than the X-ray temperature routinely show structure in velocity space which indicates that the temperature discrepancy is due to projection of multiple cluster subclumps along the line-of-sight.

Acknowledgements. We wish to thank Simon White and Peter Schneider for many useful comments. This work was supported in part by the Sonderforschungsbereich SFB 375-95 of the Deutsche Forschungsgemeinschaft.

References

- Bahcall, N.A., & Lubin, L.M. 1994, ApJ, 426, 513
 Bartelmann, M., & Weiss, A. 1994, A&A, 287, 1
 Bartelmann, M., Steinmetz, M., & Weiss, A. 1995, A&A 297, 1

- Bartelmann, M. 1995, *A&A*, 299, 11
- Bartelmann, M., Narayan, R., Seitz, S., & Schneider, P. 1996, *ApJ Letters*, in press
- Binney, J., & Tremaine, S. 1987, *Galactic Dynamics* (Princeton: University Press)
- Bonnet, H., Mellier, Y., & Fort, B. 1994, *ApJ*, 427, L83
- Briel, U.G., & Henry, J.P. 1994, *Nat*, 372, 439
- Broadhurst, T.J., Taylor, A.N., & Peacock, J.A. 1995, *ApJ*, 438, 49
- Bryan G.L., Cen R., Norman M.L., Ostriker J.P., & Stone J.M. 1994, *ApJ*, 428, 405
- Cavaliere, A., & Fusco-Femiano, R. 1976, *A&A*, 49, 137
- Cen R., & Ostriker J.P. 1994, *ApJ* 429, 4
- Cole, S., & Lacey, C. 1995, *SISSA preprint astro-ph/9510147*
- Daines, S., Jones, C., Forman, W. & Tyson, J.A. 1996, *ApJ*, submitted
- David, L.P., Harnden Jr., F.R., Kearns, K.E., & Zombeck, M.V. 1993, *U.S. ROSAT Science Data Center / Smithsonian Astrophysical Observatory*
- Edge, A.C., & Stewart, G.C. 1991, *MNRAS*, 252, 428
- Evrard, A.E. 1990, *ApJ*, 363, 349
- Evrard, A.E., Metzler, C.A., & Navarro, J.F. 1995, *SISSA preprint astro-ph/9510058*
- Gingold, R.A., & Monaghan, J.J. 1977, *MNRAS*, 181, 375
- Henriksen, M.J., & Mushotzky, R. 1985, *ApJ*, 292, 441
- Henry, J.P., & Briel, U.G. 1995, *ApJ*, 443, L9
- Jones, C., & Forman, W. 1984, *ApJ*, 276, 38
- Kaiser, N., & Squires, G. 1993, *ApJ*, 404, 441
- Katz, N., & White, S.D.M. 1993, *ApJ*, 412, 455
- King, I.R. 1966, *AJ*, 71, 64
- Lubin, L.M., & Bahcall, N.A. 1993, *ApJ*, 415, L17
- Lucy, L. 1977, *AJ*, 82, 1013
- Markevitch, M., Mushotzky, R., Inoue, H., Yamashita, K., Furuzawa, A., & Tawara, Y. 1996, *ApJ*, 456, 437
- Miralda-Escudé, J., & Babul, A. 1995, *ApJ*, 449, 18
- Monaghan, J.J. 1992, *ARA&A*, 30, 543
- Navarro, J.F., Frenk, C.S., & White, S.D.M. 1995a, *MNRAS*, 275, 720
- Navarro, J.F., Frenk, C.S., & White, S.D.M. 1995b, *MNRAS*, in press
- Sarazin, C. 1986, *Rev. Mod. Phys.*, 58, 1
- Schindler, S., & Müller, E. 1993, *A&A*, 272, 137
- Schneider, P., Ehlers, J., & Falco, E.E. 1992, *Gravitational Lenses* (Heidelberg: Springer)
- Seitz, C., & Schneider, P. 1995, *A&A*, 297, 287
- Seitz, S., & Schneider, P. 1996, *A&A*, 305, 383
- Serlemitsos, P.J., Jalota, L., Soong, Y., Kunieda, H. et al. 1995, *PASJ*, 47, 105
- Snowden, S.L., Freyberg, M.J., Plucinsky, P.P., Schmitt, J.H.M.M. et al. 1995, *ApJ*, 454, 643
- Squires, G., & Kaiser, N. 1995, *SISSA preprint astro-ph/9512094*
- Steinmetz, M. 1996, *MNRAS*, 278, 1005
- Takahashi, T., Markevitch, M., Fukazawa, Y., Ikebe, Y., Ishisaki, Y., Kikuchi, K., Makishima, K., & Tawara, Y. 1995, *ASCA Newsletter*, No. 3 (NASA/GSFC)
- Tanaka, Y., Inoue, H., & Holt, S.S. 1994, *Pub. Astr. Soc. Japan*, 46, L37
- Teague, P.F., Carter, D., & Gray, P.M. 1990, *ApJS*, 72, 715
- Thomas, P.A., & Couchman, H.M.P. 1992, *MNRAS*, 257, 11
- White, D.A., & Fabian, A.C. 1995, *MNRAS*, 273, 72
- White, S.D.M., 1994, *Les Houches Lectures*
- White, S.D.M., Efstathiou, G., & Frenk, C.S. 1993, *MNRAS*, 262, 1023
- White, S.D.M., Navarro, J.F., Evrard, A.E., & Frenk, C.S. 1993, *Nat*, 366, 429
- Wilson, G., Cole, S., & Frenk, C. 1995, *SISSA preprint astro-ph/9601102*
- Zwicky, F. 1933, *Helv. Phys. Acta*, 6, 110